nature nanotechnology

ARTICLES

PUBLISHED ONLINE: 26 JUNE 2017 | DOI: 10.1038/NNANO.2017.105

Magnetic brightening and control of dark excitons in monolayer WSe_2

Xiao-Xiao Zhang[1,2,3], Ting Cao[4,5], Zhengguang Lu[6,7], Yu-Chuan Lin[8], Fan Zhang[9], Ying Wang[6,7], Zhiqiang Li[6], James C. Hone[9], Joshua A. Robinson[8], Dmitry Smirnov[6], Steven G. Louie[4,5] and Tony F. Heinz[2,3]*

Monolayer transition metal dichalcogenide crystals, as direct-gap materials with strong light–matter interactions, have attracted much recent attention. Because of their spin-polarized valence bands and a predicted spin splitting at the conduction band edges, the lowest-lying excitons in WX_2 (X = S, Se) are expected to be spin-forbidden and optically dark. To date, however, there has been no direct experimental probe of these dark excitons. Here, we show how an in-plane magnetic field can brighten the dark excitons in monolayer WSe_2 and permit their properties to be observed experimentally. Precise energy levels for both the neutral and charged dark excitons are obtained and compared with *ab initio* calculations using the GW-BSE approach. As a result of their spin configuration, the brightened dark excitons exhibit much-increased emission and valley lifetimes. These studies directly probe the excitonic spin manifold and reveal the fine spin-splitting at the conduction band edges.

The electronic and optical properties of ultrathin transition metal dichalcogenide (TMDC) crystals in the MX_2 (M = Mo, W; X = S, Se) family have been the subject of recent interest. These 2D semiconductors exhibit a direct bandgap at monolayer thickness[1,2], have strong and anomalous excitonic interactions[3–5], and offer the potential for highly efficient light emission. The materials also provide an ideal platform for access to the valley degree of freedom, since the optical selection rules provide a simple means of controlling valley excitation[6–8]. The coupling of the spin and valley degrees of freedom in the valence band (VB) has, moreover, been recognized as another distinctive feature of the monolayer TMDC systems[7].

Despite important recent advances in our understanding of the electronic and optical properties of these materials, the nature of the spin splitting in the conduction bands (CBs) has yet to be fully elucidated by experiment. This information is essential for understanding the radiative properties of the materials, since allowed optical transitions in semiconductors occur without change in the spin of the electron. As a result, when the electron spins are polarized along the out-of-plane (z) direction, excitons with zero spin ($S_z = 0$, corresponding to bands with the same electron spin) are bright, while excitons with non-zero spin ($S_z = \pm 1$, corresponding to bands with opposite spin) are dark. (The spin of the hole is opposite to that of the electron for a given band state. In this Article, the bright state refers to the 1s exciton with $S_z = 0$ and spin-allowed transitions; the dark state to the 1s exciton with $S_z = \pm 1$ and spin-forbidden transitions.) In TMDCs, the CBs have been theoretically predicted to be fully spin polarized[9–11] just like the more strongly split VBs. The spin splitting of the CBs is expected to be relatively modest, with a size comparable to room-temperature thermal energy and, significantly, exhibiting different signs (compared to the valence band splitting) depending on the chemical composition of the TMDC crystal. Specifically, in Mo compounds, electrons in the lowest CB are expected to have the same spin as those in the highest VB. In contrast, the opposite spin ordering is expected in W compounds (Fig. 1b), and, correspondingly, the lowest energy exciton is expected to be optically dark. The existence of this lower-lying dark state will quench light emission, particularly at low temperatures. Although distinct behaviour for the thermal activation of light emission has been observed in different TMDC monolayer semiconductors[12–14], experiments have not revealed the exact energy structure of the excitonic states. The latter is of critical importance for valley and spin transport and of their manipulation in these systems.

Here, we mixed the spin components of the exciton states in monolayer WSe_2 through the application of an in-plane magnetic field. This perturbation brightens the dark exciton states and allows us to observe light emission directly from these otherwise inaccessible states (In a study utilizing coupling to the out-of-plane transition dipole moment by surface plasmon polaritons, similar signatures of dark excitons have also recently been observed[15]). With a spectroscopic signature of the dark excitons, we measured the splitting between the originally bright and dark states with high precision. In the presence of free charge carriers in the WSe_2 crystal, trions (charged excitons) also form[16]. The corresponding dark trion states also become visible with magnetic brightening. Our spectroscopic determination of the energies for the manifold of dark and bright excitonic states agrees well with our predictions of *ab initio* theory using the GW-BSE formalism. Interestingly, the energy splitting between the bright and dark charged excitons differs from that for the neutral excitons, reflecting the role of many-body interactions beyond the single-particle

[1]Department of Physics, Columbia University, New York, New York 10027, USA. [2]Department of Applied Physics, Stanford University, Stanford, California 94305, USA. [3]SLAC National Accelerator Laboratory, 2575 Sand Hill Road, Menlo Park, California 94025, USA. [4]Department of Physics, University of California, Berkeley, California 94720, USA. [5]Materials Sciences Division, Lawrence Berkeley National Laboratory, 1 Cyclotron Road, Berkeley, California 94720, USA. [6]National High Magnetic Field Laboratory, Tallahassee, Florida 32312, USA. [7]Department of Physics, Florida State University, Tallahassee, Florida 32310, USA. [8]Department of Materials Science and Engineering and Center for 2-Dimensional and Layered materials, The Pennsylvania State University, University Park, Pennsylvania 16802, USA. [9]Department of Mechanical Engineering, Columbia University, New York, New York 10027, USA. *e-mail: tony.heinz@stanford.edu

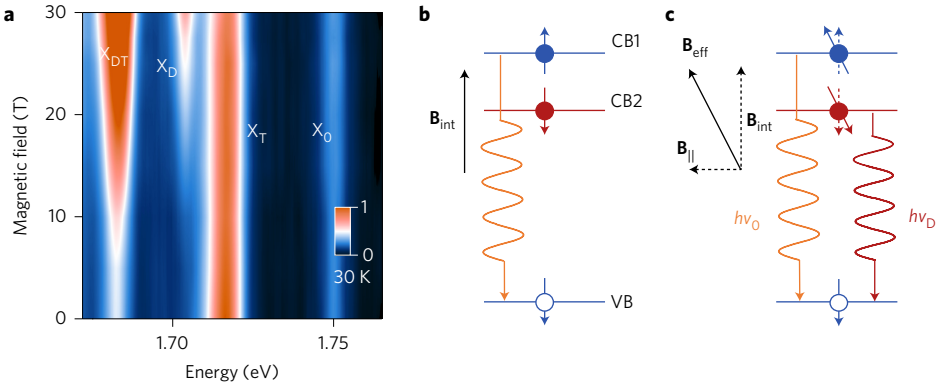

Figure 1 | Conduction band structure of monolayer WSe_2 and magnetic brightening of dark excitons. a, False-colour plot of the measured emission spectrum for monolayer WSe_2 at a temperature of 30 K as a function of the strength of the applied $B_{||}$. The displayed energy range includes emission from the neutral A exciton (X_0) and the associated trion state (X_T). Emission features from the dark exciton (X_D) and dark trion (X_{DT}) grow with increasing $B_{||}$. The scale bar represents the normalized photoluminescence intensity. **b**, For monolayer WSe_2, electrons in the lower conduction band (CB2) have spin opposite that in the upper valence band (VB), rendering the lowest transition optically dark. Only transitions from the upper CB (at energy $h\nu_0$) are allowed. The spin-split CB bands, CB1 and CB2, can be described as the result of an effective out-of-plane magnetic field $\mathbf{B}_{int}$ acting on the electron magnetic moment. The blue and red lines represent bands with electrons' spin up and down, respectively. The arrows indicate the spin of the electron/hole in an excitonic state. **c**, Under an external in-plane magnetic field $\mathbf{B}_{||}$, the total effective field $\mathbf{B}_{eff} = \mathbf{B}_{int} + \mathbf{B}_{||}$ is tilted away from the surface normal, resulting in tilted spin polarization of the CB electrons. Optical transitions at energy $h\nu_D$ from an exciton formed mainly from the lower CB and corresponding to the dark exciton then become weakly allowed.

picture. Analysis of the splittings provides quantitative information about the CB band structure and many-body interactions in these materials.

Brightening the dark excitons allows us to explore the dynamics and valley properties of these states. Unlike their bright counterparts, we can dramatically alter the radiative lifetime of the dark states by tuning the strength of the applied magnetic field and thus explore states with lifetimes orders-of-magnitude longer than those intrinsic to the bright states. Moreover, the measured valley lifetime of the dark excitons, protected from intervalley exchange scattering by their spin configuration, is also significantly longer than the valley lifetime of bright excitons. Such increased radiative and valley lifetimes are desirable for the development of valleytronic devices, as they facilitate encoding, storage and manipulation of valley information[7,17].

Emergence of dark excitons under $B_{||}$

In our experiment, we directly observed the emergence of dark states with application of an in-plane magnetic field. The colour plot (Fig. 1a) provides an overview of the photoluminescence (PL) spectra from an exfoliated WSe_2 monolayer for in-plane magnetic fields up to $B_{||} = 31$ T. Two new states, labelled X_D and X_{DT}, are seen to emerge and become progressively more intense with increasing field. We first present a qualitative picture of how an in-plane magnetic field serves to brighten the spin-forbidden dark exciton states.

The spin–orbit-induced splitting of the CB can be attributed to an effective internal magnetic field $\mathbf{B}_{int}$, oriented perpendicular to the plane of the 2D layer and acting on the electron spin (Fig. 1b). If we apply an external in-plane magnetic field $\mathbf{B}_{||}$, the total effective magnetic field acting on the CB electrons, $\mathbf{B}_{eff} = \mathbf{B}_{int} + \mathbf{B}_{||}$, is now tilted away from the normal direction by an angle $\sim B_{||}/B_{int}$ in small $B_{||}$ limit (Fig. 1c). Since the expected spin splitting of CBs of a few tens of millielectronvolts[9,10] corresponds to B_{int} of hundreds of teslas, an appreciable tilt angle is achievable for $B_{||}$ of tens of teslas. On the other hand, the spin splitting in the VBs is ~10 times greater than in the CBs. B_{int} is correspondingly larger for the VBs, and the tilting of $\mathbf{B}_{eff}$ for VBs can be neglected. Consequently, $\mathbf{B}_{||}$ causes the spin state of electrons in the lower CB to have a finite projection on the zero-field state in the upper VB, and radiative recombination becomes weakly allowed for this otherwise forbidden transition (Fig. 1b). We note that while an out-of-plane magnetic field causes measurable Zeeman shifts[18–20] and Landau quantization of valleys[21], the in-plane field produces only very minor Zeeman shifts (Supplementary Section 7) and does not couple to the in-plane motion of electrons. The in-plane field thus allows us to probe directly the effects of spin mixing. Although the oscillator strength induced in the dark exciton by $\mathbf{B}_{||}$ remains small, emission from the brightened dark states can still be significant at low temperature as a result of the large occupation number of the lower-lying dark state. In-plane magnetic fields have also been used to brighten optically dark excitons in quantum dots[22], carbon nanotubes[23] and quantum wells[24], although the physical mechanisms differ.

Figure 2 shows detailed PL spectra for different values of the applied magnetic field $B_{||}$. In the absence of the field, four peaks are visible: the highest-energy peak (X_0) arising from the optically allowed transition of the neutral A exciton; the associated trion state (X_T) due to the presence of unintentional doping of the sample[16]; and two lower-energy peaks (L1 and L2), attributed to localized excitons from defect states[16,25,26]. As $B_{||}$ is increased, two additional peaks, labelled X_D and X_{DT}, emerge and become prominent at high field strengths. The originally bright states, by contrast, show little response to the applied field. As will be justified in detail below, we assign the additional peaks to emission from the neutral dark exciton (X_D) and the charged dark exciton (X_{DT}). The WSe_2 emission spectrum is simplified at higher sample temperatures where the localized exciton states are absent and the trion feature becomes less prominent. At a temperature of 100 K with $B_{||} = 31$ T (Fig. 2b), we see the emergence of the neutral dark exciton X_D in the absence of the defect emission peaks. The inset of Fig. 2b shows that the extracted X_D feature has essentially the same width as that of the X_0 peak, which, we note, is significantly smaller than that of the trion. The energy shift between the X_0 and X_D features also agrees with that observed in the low-temperature data presented above. Additional PL spectra for temperatures between 4 K and 140 K are presented in Supplementary Section 2.

Our experimental observations strongly support the assignment of the X_D and X_{DT} peaks as emission from neutral and charged dark exciton emission associated with the split CBs. First, their

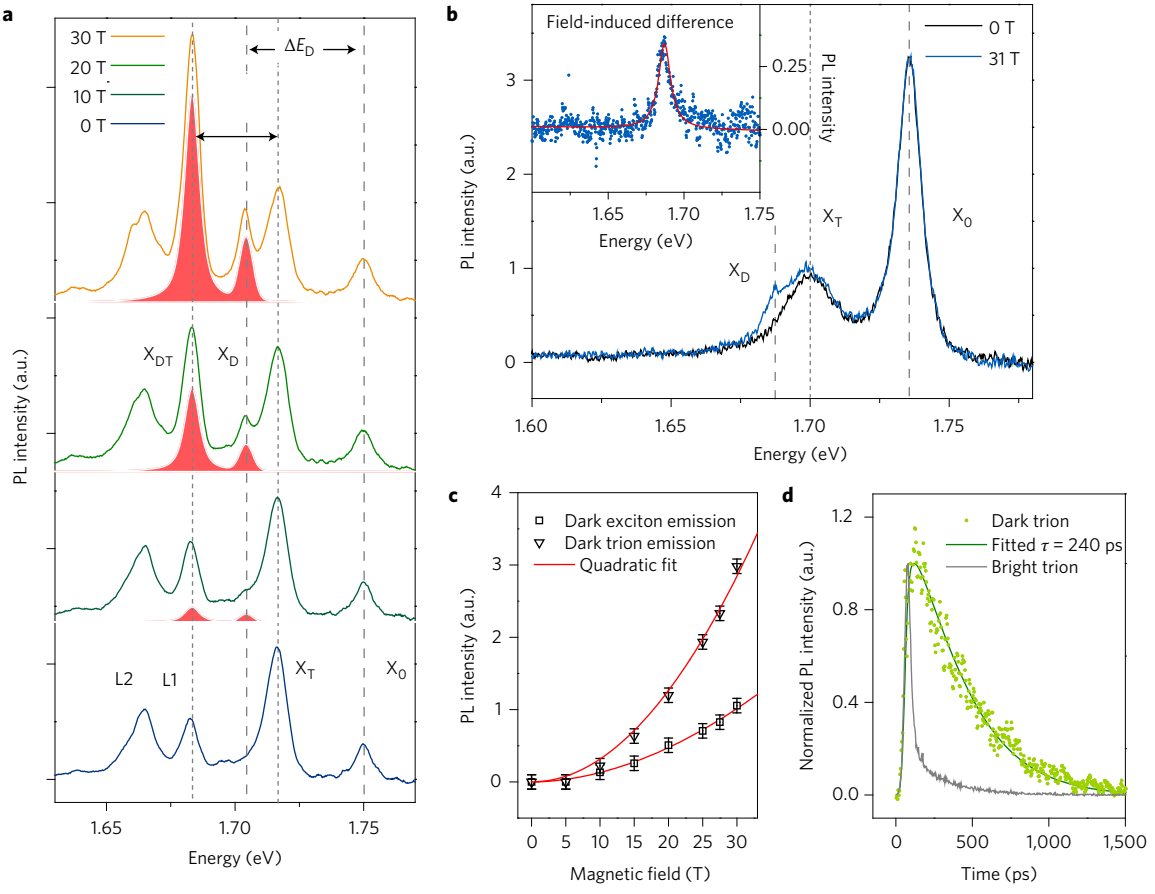

Figure 2 | Magnetic field-dependence of emission from dark exciton states. a, PL spectra for selected strengths of the in-plane magnetic field $B_{||}$ at a temperature of $T = 30$ K. For $B_{||} = 0$, the spectrum shows emission from the neutral exciton X_0 (1.750 eV), the trion X_T (1.716 eV), and localized excitonic states L_1 and L_2. These features remain unchanged with increasing $B_{||}$. Two new peaks grow in at fixed energies, the dark exciton X_D at 1.704 eV (separated by energy ΔE_D from X_0) and the dark trion X_{DT} at 1.683 eV (separated by energy ΔE_{DT} from X_T). **b**, PL spectra at $T = 100$ K for $B_{||} = 0$ and 31 T. For $B_{||} = 0$, the spectrum is dominated by the neutral exciton, with a weaker trion feature. For $B_{||} = 31$ T, the X_D peak emerges, while the X_{DT} emission is too weak to observe. The X_D feature has essentially the same linewidth as X_0 (inset), which is about half of the linewidth of the X_T feature. **c**, The PL intensity of the dark exciton and dark trion as a function of $B_{||}$ at $T = 30$ K. Both features increase quadratically with $B_{||}$. The error bars represent the uncertainty in fitting the integrated PL intensity. **d**, Comparison of time-resolved PL from the bright and dark trion under excitation by femtosecond laser pulses for $T = 4$ K and $B_{||} = 17.5$ T. The trace of the fast bright trion emission (<20 ps) is limited by the system instrument response function. The dark trion emission decay (~230 ps) is plotted by extracting the magnetic field-induced difference at the energy of the X_{DT} feature.

emergence depends only on the magnitude of the in-plane magnetic field, while an out-of-plane field causes only Zeeman energy shifts of the original emission features, without the induction of additional emission peaks (Supplementary Section 3), as reported previously in the literature[27]. Second, the PL intensities of both the X_D and X_{DT} features increase quadratically with $B_{||}$ (Fig. 2c). This is expected for brightened emission from a spin-forbidden transition: the magnetic field $B_{||}$ mixes the wavefunction of CB2 with a component from CB1 that is linear in $B_{||}$. A quadratic increase of the dark exciton oscillator strength with $B_{||}$ is then expected, as discussed in detail below. Third, the energies of the emission peaks are independent of $B_{||}$, consistent with a theoretically predicted Zeeman shift of <0.1 meV for $B_{||}$ up to 31 T (Supplementary Section 7). Fourth, the dark state features are observed in both exfoliated samples and monolayers grown by chemical vapour deposition, despite the differences in material defects (Supplementary Section 2). In a comparative study, we investigated $MoSe_2$ monolayers, in which the CB spin splitting is predicted to have the opposite sign. For the case of $MoSe_2$, the emission spectrum exhibits no meaningful response to the application of an in-plane magnetic field $B_{||}$ (Supplementary Section 4). This latter result is expected, since the dark excitons in this system are predicted to lie at energies above the corresponding bright states. The dark exciton states in $MoSe_2$ will then have low thermal population and emission.

We further investigated the emission dynamics of the dark states using time-resolved photoluminescence (TRPL). In Fig. 2d, we contrast the emission dynamics for bright and dark trion states (emission from the neutral exciton was too weak for accurate TRPL measurement with the available $B_{||} = 17.5$ T). The dark trion emission exhibits a lifetime of 230 ± 10 ps, while the bright trion lifetime is less than 20 ps. In our analysis of the dark trion dynamics in Fig. 2d, we subtracted the background emission from the L1 defect (measured at $B_{||} = 0$). The validity of this approach is substantiated by a global fitting analysis of magnetic field-dependent TRPL traces presented in Supplementary Section 6. We discuss later the physical origin and significance of the long lifetime of dark states.

Theoretical investigation of energy splittings

We now discuss the energy shifts of the dark exciton and dark trion relative to the corresponding bright states. Based on the spectra presented above, as well as additional results over a more extended temperature range of 4 K to 140 K (Supplementary Section 2), we find a bright–dark splitting of $\Delta E_D = 47 \pm 1$ meV for the neutral exciton. A similar analysis of the bright–dark splitting for the

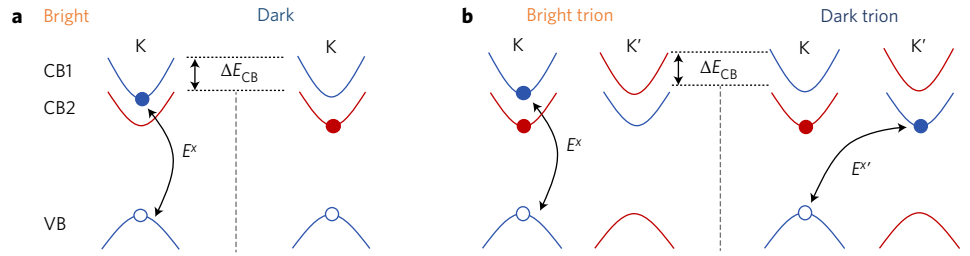

Figure 3 | Schematic illustration of bright and dark neutral and charged excitonic states. The blue and red lines represent spin-up and spin-down bands, respectively. **a**, The spin-valley configuration of neutral bright and dark excitons. ΔE_{CB} denotes the energy splitting of the two CBs. The black line represents the e-h exchange interaction E^x for the ($S_z = 0$) bright exciton, which is absent for the ($S_z = \pm 1$) dark exciton. **b**, Spin-valley configuration of the lowest-energy n-type bright and dark trion states. An e-h exchange interaction E^x is present for the intervalley ($S_z = 0$) e-h pair, as shown.

trion states yields $\Delta E_{DT} = 32 \pm 1$ meV. These values, being comparable to the room-temperature thermal energy, are consistent with the observed strong suppression of PL at low temperatures[12–14].

The peak shifts ΔE_D and ΔE_{DT} both reflect the splitting ΔE_{CB} between the two underlying conduction bands (CB1 and CB2 in Figs 1 and 3). They are, however, also affected by the difference in exciton binding energies between the corresponding bright and dark states. Let us first consider how these factors play out for the case of the neutral bright and dark exciton. Using the BerkeleyGW package[28], we applied the *ab initio* GW-BSE approach[29,30] to calculate the quasiparticle band structure and excitonic states in monolayer WSe_2. Our calculation shows that the binding energy difference between the bright and dark 1*s* excitons is 17 meV. As the calculated wavefunctions of the bright and dark excitons exhibit very similar radial distributions (Supplementary Fig. 14), we can examine the difference in binding energy using perturbation theory (see Supplementary Section 7 for details). We find that we can account for the difference in terms of two factors: the different spin configuration of the bright and dark excitons, and the different effective masses of electrons in CB1 and CB2. For the former, relative to the $S_z = \pm 1$ dark exciton, the $S_z = 0$ bright exciton experiences an additional repulsive electron–hole (e–h) exchange interaction, which shifts the bright exciton energy upwards by E^x (Fig. 3a). For the latter, from the quasiparticle band structure, CB2 in WSe_2 has a larger mass than higher-lying CB1 (Supplementary Section 7). This leads to an increased binding energy for the dark exciton; we denote the corresponding mass-induced shift as δE_0. Including the band splitting with the two many-body corrections, the bright–dark neutral exciton shift is $\Delta E_D \approx \Delta E_{CB}$ (40 meV) + E^x (6 meV) + δE_0 (11 meV). For the overall shift, we obtain a value of $\Delta E_D = 57$ meV from our *ab initio* GW-BSE calculations, in good agreement with the experimental value of 47 meV.

For the bright and dark states of the trion, we need to consider additional many-body effects in this three-body correlated state. For n-type trions, which are relevant for our experiment, the expected lowest-energy configurations for the bright and dark states are shown in Fig. 3b, as dictated by having different electron valley–spin configurations. (Based on the observed spectral shift between X_0 and X_T, which differs for n- and p-type trions, we infer that we have n-type trions in our samples[16]. For completeness, we provide an analysis for p-type trions in the Supplementary Information.) ΔE_{CB} still gives the same single-particle contribution to ΔE_{DT}. However, unlike the neutral excitons, both the bright and dark trions experience e–h exchange interactions (Fig. 3b)—in the bright case, an intravalley exchange (E^x) and, in the dark case, an intervalley exchange interaction ($E^{x'}$). As the e–h wavefunction overlap of the $S_z = 0$ exciton is almost identical for the intervalley and intravalley configurations, our calculation indicates that E^x and $E^{x'}$ are very similar (within ~1 meV). Therefore ΔE_{DT} can be approximated as $\Delta E_{DT} \approx \Delta E_{CB} + \delta E_T$, where δE_T is the mass-induced binding energy difference between the bright and dark trions. Because δE_T is expected to be smaller than δE_0, we expect—and observe experimentally—that ΔE_D exceeds ΔE_{DT}.

From the experimental data and above analysis, we can estimate the CB splitting from our measurements to mitigate the uncertainty of the splitting predicted by theory[9,10,31,32]. If we assume a mass-induced binding energy difference of $\delta E_T = 0.5\delta E_0$, a first-order approximation based on averaging the electron band masses for the trion states, we then have $\Delta E_D - \Delta E_{DT} \approx E^x + \delta E_T$. Taking our experimental data, and noting that $E^x > 0$, we obtain a possible range of CB splittings of 17 meV $< \Delta E_{CB} <$ 32 meV. Further, using the theoretical estimate of $\delta E_T \approx 6$ meV, we obtain $\Delta E_{CB} \approx 26$ meV from the relation $\Delta E_{DT} \approx \Delta E_{CB} + \delta E_T$ introduced above.

Radiative and valley lifetimes of dark excitons

We now demonstrate how this approach also serves to create new excitonic states with tunable properties. Bright excitons in monolayer TMDC materials exhibit exceptionally short (picosecond to subpicosecond) intrinsic radiative lifetimes, $\tau_{rad-B}(T = 0)$, where T is temperature, as a consequence of their unusually large binding energies[33]. On the other hand, a long and tunable exciton radiative lifetime would be attractive for many purposes; brightened dark excitons offer just this possibility. Experimentally, we see evidence for a long radiative lifetime of the brightened dark states in our TRPL measurements (Fig. 2d).

Here, we provide a quantitative description of the effect of the applied $B_\parallel$ on the dark excitons' radiative properties. Since the magnetic field-induced mixing occurs predominantly between pairs of dark and bright states, an effective two-level model captures the underlying physics. The influence of $B_\parallel$ is, moreover, quite simple because it does not couple to the in-plane motion of electrons, but only to their spin magnetic moment. In the weak-field limit, this model predicts a field-induced oscillator strength for the dark excitons $f_D(B_\parallel) = (\mu_B B_\parallel/\Delta E_D)^2 f_0$, where f_0 is the field-free bright exciton oscillator strength, ΔE_D is the bright–dark state splitting and μ_B is the Bohr magneton (details in Supplementary Section 7). This relation immediately explains the observed quadratic dependence of the PL with $B_\parallel$ (Fig. 2c) under our experimental conditions where non-radiative relaxation of the excitons dominates (and the relaxation channels are not significantly altered by the magnetic field). For the highest applied field of $B_\parallel = 31$ T, we predict only a slight brightening of dark excitons of $f_D \approx 1.4 \times 10^{-3} f_0$. As the lower-energy state, dark excitons with such small oscillator strength can, however, still dominate in PL (Fig. 2a) because of their much larger occupation at low temperature. Assuming thermal equilibrium occupation numbers, we can, for example, estimate the dark exciton oscillator strength from the observed strength of the dark exciton compared with the bright exciton for $B_\parallel = 31$ T at 100 K (Fig. 2b). We infer $f_D \approx 4 \times 10^{-4} f_0$ (see Supplementary Section 7 for details), a value comparable to the prediction of the analysis given above. Moreover, we can

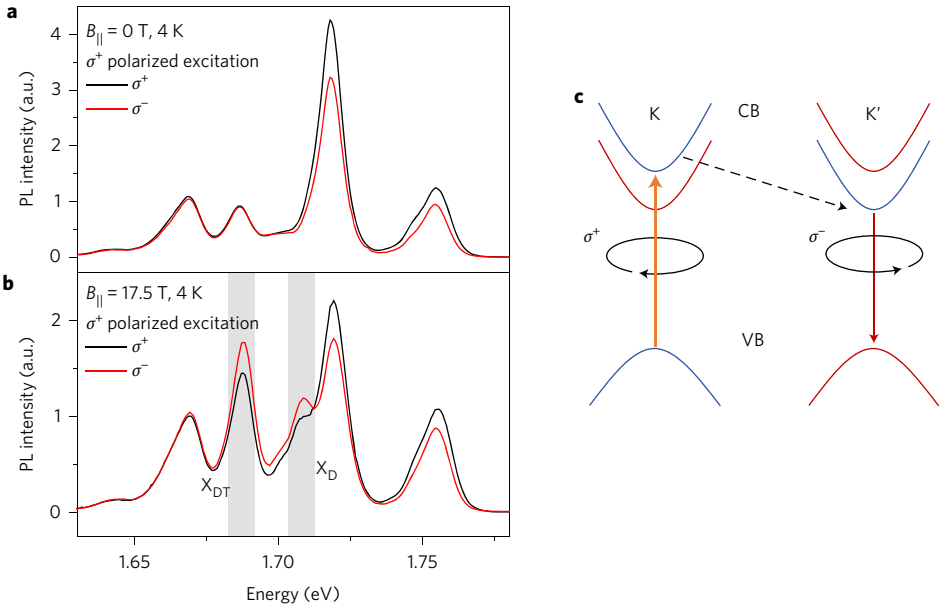

Figure 4 | Valley properties of dark excitons based on polarized PL. a,b, At a sample temperature of 4 K, emission spectra resolved into circularly polarized components are shown for near-resonant excitation (1.88 eV) of the bright exciton with σ^+ circular polarized radiation for in-plane magnetic fields of $B_{||} = 0$ (**a**) and $B_{||} = 17.5$ T (**b**). For $B_{||} = 0$ (**a**), the neutral and trion states exhibit enhanced circular polarization in emission matching that of the excitation, and the lower-energy defect-related states show negligible circular polarization. For $B_{||} = 17.5$ T (**b**), the polarization of the bright states remains essentially unchanged. The new dark exciton X_D and dark trion X_{DT} emission features, on the other hand, show circular polarized emission, but with the opposite handedness. **c**, A schematic representation of relaxation through a spin-conserving intervalley electron scattering process.

estimate the effective radiative lifetime of the brightened dark excitons from the ratio f_D/f_0 and the bright-exciton effective radiative lifetime $\tau_{rad-B}(T)$. Taking the previously reported 150 fs (ref. 33) as the intrinsic $\tau_{rad-B}(T = 0)$, we predict $\tau_{rad-D} = 28$ ns for $B_{||} = 17.5$ T at 4 K, corresponding to the conditions of Fig. 2d (Supplementary Section 7). This radiative lifetime is consistent with our measured emission time of 230 ps and the material's low quantum efficiency. For $B_{||} = 10$ T and $T = 50$ K, where we can still observe the dark state emission, we predict $\tau_{rad-D}(T = 50\ K) > 1$ μs. For improved crystals exhibiting higher quantum efficiency and narrower emission features, one would be able to observe dark states with still longer radiative lifetimes. We can thus achieve wide tuning of effective radiative lifetimes under conditions where the brightened dark states are readily observable.

As a final area of exploration, we note that optical access to the valley degree of freedom and the inherent coupling of the valley and spin degrees of freedom in the TMDC monolayers are among the most interesting and distinctive properties of these materials[7]. We have consequently also examined the valley properties of the magnetically brightened dark states. Since the optical valley selection rules reflect the character of the underlying band states, they should also be obeyed for the magnetically brightened dark states, thus providing a means of probing the valley degree of freedom. Results of such a measurement are presented in Fig. 4. For the bright states, we see enhancement of the emission with the same handedness (Fig. 4a,b), in accord with previous reports[16,26]. For emission from the two brightened dark states (shaded grey areas in Fig. 4b), we also observe partial circular polarization, but the opposite handedness. This intriguing result reflects the distinctive nature of the dark excitons. Although the precise mechanism behind this observation remains unclear, we note that the creation of the dark excitons is expected to occur through relaxation of bright excitons by scattering of electrons into the lower CBs, either through an intervalley or intravalley scattering process. We expect the intervalley process, not requiring a spin flip, to be more efficient. Photoexcitation in one valley thus gives rise to a higher population of photogenerated electrons in the lowest CB in the other valley, which may explain the observed opposite circularly polarized emission.

The fact that the dark state exhibits circularly polarized emission also has implications for the valley lifetime of this state. Taking the experimental dark trion exciton emission time of ~230 ps (Fig. 2d), together with its measured degree of circular polarization, we infer a dark state valley lifetime exceeding 60 ps. This value significantly exceeds the valley lifetime of the bright excitons[34,35], in which intervalley exciton exchange between the K and K' valleys is likely to play a crucial role in depolarization[36–39]. Scattering of dark excitons between the different valleys would require an additional spin flip, making such exchange coupling much less efficient. The valley character of dark states is thus protected by their spin configuration.

Conclusion

The approach of magnetic brightening described here has yielded a direct spectroscopic determination of the energies of spin-forbidden dark excitonic states in a model TMDC monolayer, as well as important information about the CB splitting. Magnetic brightening of dark excitons also provides a route to produce optically observable states with long and widely tunable radiative lifetimes, as well as greater valley stability compared with bright excitons. These characteristics permit new approaches to store and manipulate photoexcited valley and spin information. The enhanced radiative and valley lifetimes, combined with the exceptionally strong many-body interactions present in these systems, offers, moreover, a promising platform to realize correlated exciton states, such as Bose–Einstein condensates.

Methods

Methods and any associated references are available in the online version of the paper.

Received 24 January 2017; accepted 26 April 2017;
published online 26 June 2017

References

1. Splendiani, A. *et al.* Emerging photoluminescence in monolayer MoS_2. *Nano Lett.* **10,** 1271–1275 (2010).
2. Mak, K. F., Lee, C., Hone, J., Shan, J. & Heinz, T. F. Atomically thin MoS_2: a new direct-gap semiconductor. *Phys. Rev. Lett.* **105,** 136805 (2010).
3. Ye, Z. *et al.* Probing excitonic dark states in single-layer tungsten disulphide. *Nature* **513,** 214–218 (2014).
4. Chernikov, A. *et al.* Exciton binding energy and nonhydrogenic Rydberg series in monolayer WS_2. *Phys. Rev. Lett.* **113,** 076802 (2014).
5. Qiu, D. Y., da Jornada, F. H. & Louie, S. G. Optical spectrum of MoS_2: many-body effects and diversity of exciton states. *Phys. Rev. Lett.* **111,** 216805 (2013).
6. Xiao, D., Liu, G.-B., Feng, W., Xu, X. & Yao, W. Coupled spin and valley physics in monolayers of MoS_2 and other group-VI dichalcogenides. *Phys. Rev. Lett.* **108,** 196802 (2012).
7. Xu, X., Yao, W., Xiao, D. & Heinz, T. F. Spin and pseudospins in layered transition metal dichalcogenides. *Nat. Phys.* **10,** 343–350 (2014).
8. Cao, T. *et al.* Valley-selective circular dichroism of monolayer molybdenum disulphide. *Nat. Commun.* **3,** 887 (2012).
9. Liu, G.-B., Shan, W.-Y., Yao, Y., Yao, W. & Xiao, D. Three-band tight-binding model for monolayers of group-VIB transition metal dichalcogenides. *Phys. Rev. B* **88,** 085433 (2013).
10. Kormányos, A. *et al.* K·p theory for two-dimensional transition metal dichalcogenide semiconductors. *2D Mater.* **2,** 022001 (2015).
11. Zhu, Z. Y., Cheng, Y. C. & Schwingenschlögl, U. Giant spin-orbit-induced spin splitting in two-dimensional transition-metal dichalcogenide semiconductors. *Phys. Rev. B* **84,** 153402 (2011).
12. Zhang, X.-X., You, Y., Zhao, S. Y. F. & Heinz, T. F. Experimental evidence for dark excitons in monolayer WSe_2. *Phys. Rev. Lett.* **115,** 257403 (2015).
13. Withers, F. *et al.* WSe_2 light-emitting tunneling transistors with enhanced brightness at room temperature. *Nano Lett.* **15,** 8223–8228 (2015).
14. Wang, G. *et al.* Spin-orbit engineering in transition metal dichalcogenide alloy monolayers. *Nat. Commun.* **6,** 10110 (2015).
15. Zhou, Y. *et al.* Probing dark excitons in atomically thin semiconductors via near-field coupling to surface plasmon polaritons. *Nat. Nanotech.* http://dx.doi.org/10.1038/nnano.2017.106 (2017).
16. Jones, A. M. *et al.* Optical generation of excitonic valley coherence in monolayer WSe_2. *Nat. Nanotech.* **8,** 634–638 (2013).
17. Mak, K. F., McGill, K. L., Park, J. & McEuen, P. L. Valleytronics. The valley Hall effect in MoS_2 transistors. *Science* **344,** 1489–1492 (2014).
18. Li, Y. *et al.* Valley splitting and polarization by the Zeeman effect in monolayer $MoSe_2$. *Phys. Rev. Lett.* **113,** 266804 (2014).
19. Srivastava, A. *et al.* Valley Zeeman effect in elementary optical excitations of monolayer WSe_2. *Nat. Phys.* **11,** 141–147 (2015).
20. MacNeill, D. *et al.* Breaking of valley degeneracy by magnetic field in monolayer $MoSe_2$. *Phys. Rev. Lett.* **114,** 037401 (2015).
21. Wang, Z., Shan, J. & Mak, K. F. Valley-and spin-polarized Landau levels in monolayer WSe_2. *Nat. Nanotech.* **12,** 144–149 (2016).
22. Bayer, M., Stern, O., Kuther, A. & Forchel, A. Spectroscopic study of dark excitons in $In_xGa_{1-x}As$ self-assembled quantum dots by a magnetic-field-induced symmetry breaking. *Phys. Rev. B* **61,** 7273–7276 (2000).
23. Zaric, S. *et al.* Optical signatures of the Aharonov-Bohm phase in single-walled carbon nanotubes. *Science* **304,** 1129–1131 (2004).
24. Glasberg, S., Shtrikman, H., Bar-Joseph, I. & Klipstein, P. Exciton exchange splitting in wide GaAs quantum wells. *Phys Rev. B* **60,** R16295 (1999).
25. Wang, G. *et al.* Valley dynamics probed through charged and neutral exciton emission in monolayer WSe_2. *Phys Rev. B* **90,** 075413 (2014).
26. You, Y. *et al.* Observation of biexcitons in monolayer WSe_2. *Nat. Phys.* **11,** 477–481 (2015).
27. Koperski, M. *et al.* Single photon emitters in exfoliated WSe_2 structures. *Nat. Nanotech.* **10,** 503–506 (2015).
28. Deslippe, J. *et al.* BerkeleyGW: a massively parallel computer package for the calculation of the quasiparticle and optical properties of materials and nanostructures. *Comput. Phys. Commun.* **183,** 1269–1289 (2012).
29. Hybertsen, M. S. & Louie, S. G. Electron correlation in semiconductors and insulators: band gaps and quasiparticle energies. *Phys. Rev. B* **34,** 5390–5413 (1986).
30. Rohlfing, M. & Louie, S. G. Electron-hole excitations and optical spectra from first principles. *Phys. Rev. B* **62,** 4927–4944 (2000).
31. Kośmider, K., González, J. W. & Fernández-Rossier, J. Large spin splitting in the conduction band of transition metal dichalcogenide monolayers. *Phys. Rev. B* **88,** 245436 (2013).
32. Echeverry, J. P., Urbaszek, B., Amand, T., Marie, X. & Gerber, I. C. Splitting between bright and dark excitons in transition metal dichalcogenide monolayers. *Phys. Rev. B* **93,** 121107 (2016).
33. Pöllmann, C. *et al.* Resonant internal quantum transitions and femtosecond radiative decay of excitons in monolayer WSe_2. *Nat. Mater.* **14,** 889–893 (2015).
34. Lagarde, D. *et al.* Carrier and polarization dynamics in monolayer MoS_2. *Phys. Rev. Lett.* **112,** 047401 (2014).
35. Zhu, C. R. *et al.* Exciton valley dynamics probed by Kerr rotation in WSe_2 monolayers. *Phys. Rev. B.* **90,** 161302 (2014).
36. Yu, T. & Wu, M. Valley depolarization due to intervalley and intravalley electron-hole exchange interactions in monolayer MoS_2. *Phys. Rev. B* **89,** 205303 (2014).
37. Hao, K. *et al.* Direct measurement of exciton valley coherence in monolayer WSe_2. *Nat. Phys.* **12,** 677–682 (2016).
38. Glazov, M. M. *et al.* Exciton fine structure and spin decoherence in monolayers of transition metal dichalcogenides. *Phys. Rev. B* **89,** 201302 (2014).
39. Dery, H. & Song, Y. Polarization analysis of excitons in monolayer and bilayer transition-metal dichalcogenides. *Phys. Rev. B* **92,** 125431 (2015).
40. Giannozzi, P. *et al.* QUANTUM ESPRESSO: a modular and open-source software project for quantum simulations of materials. *J. Phys. Condens. Matter* **21,** 395502 (2009).

Acknowledgements

Support at SLAC/Stanford was provided by the AMOS program, Chemical Sciences, Geosciences, and Biosciences Division, Basic Energy Sciences, US Department of Energy under contract no. DE-AC02-76-SFO0515 and the Betty and Gordon Moore Foundation's EPiQS Initiative through grant no. GBMF4545 (T.F.H.). for data analysis, and by Air Force Office of Scientific Research through the MURI Center for dynamic magneto-optics under grant. no. FA9550-14-1-0040 for optical measurements. The theoretical studies were supported by the Theory of Materials Program funded by the Director, Office of Science, Office of Basic Energy Sciences, Materials Sciences and Engineering Division, US Department of Energy under contract no. DE-AC02-05CH11231, which supported the GW and GW-BSE calculations, and by the National Science Foundation (NSF) grant no. DMR-1508412, which supported the magnetic-field-induced exciton mixing analyses. Computational resources were provided by the DOE at Lawrence Berkeley National Laboratory's NERSC facility and by the NSF through XSEDE resources at NICS. Y.-C.L. and J.A.R. acknowledge the support from the Center for Low Energy Systems Technology (LEAST), one of six centres supported by the STARnet phase of the Focus Center Research Program (FCRP), a Semiconductor Research Corporation program sponsored by MARCO and DARPA. Sample preparation at Columbia University was supported by the NSF MRSEC for Precision Assembly of Superstratic and Superatomic Solids through grant no. DMR-1420634. Z.L. and D.S. acknowledge the support from the US Department of Energy (grant no. DE-FG02-07ER46451) for high-field CW PL measurements that were performed at the National High Magnetic Field Laboratory, which is supported by the NSF Cooperative Agreement no. DMR-1157490 and the State of Florida.

Author contributions

X.-X.Z. and T.C. conceived the experiment. X.-X.Z. and Z.G.L. performed the experiment, with assistance from Z.Q.L., Y.W. and D.S. at the National High Magnetic Field Laboratory. T.C. performed the theoretical calculation and analysis under the guidance of S.G.L. The exfoliated samples were prepared by F.Z. under the guidance of J.C.H., and Y.-C.L. and J.A.R. prepared the chemically grown samples. Analysis and interpretation of the data were performed by X.-X.Z. and T.F.H. All authors discussed the results and contributed to the writing of the manuscript.

Additional information

Supplementary information is available in the online version of the paper. Reprints and permissions information is available online at www.nature.com/reprints. Publisher's note: Springer Nature remains neutral with regard to jurisdictional claims in published maps and institutional affiliations. Correspondence and requests for materials should be addressed to T.F.H.

Competing financial interests

The authors declare no competing financial interests.

Methods

Monolayers of WSe_2 were prepared by exfoliation from bulk crystals onto a SiO_2/Si substrate with a 300-nm-thick oxide layer. The monolayer flakes were identified by optical contrast microscopy and PL measurements. The selected monolayer was transferred onto another SiO_2/Si substrate with pre-patterned markers to facilitate optical measurements under the magnetic field. Information about the grown WSe_2 monolayers is presented in the Supplementary Information.

Optical measurements in the 31 T magnet were carried out using a fibre-based optical probe, while the polarization-resolved PL and TRPL measurements were made using free-space optics in the 17.5 T magnet. The TRPL measurements were performed by means of the time-resolved single-photon-counting technique. The excitation was provided by a frequency-doubled mode-locked Ti:sapphire (Coherent, Vitesse) laser operating at a repetition rate of 80 MHz with pulses of 300-fs duration at a wavelength of 400 nm. The collected PL was spectrally filtered by a grating monochromator (bandpass of 10 nm) and detected with an avalanche photodiode (PicoQuant, PDM) for analysis using time-resolved single photon counting (PicoQuant, PicoHarp 300). We determined the instrument response function of the TRPL set-up by using the temporal profile produced by the 800-nm femtosecond pulses from the mode-locked Ti:sapphire laser.

Theory. Density functional calculations were performed using the local density approximation (LDA) implemented in the Quantum ESPRESSO package[40]. We assumed the experimental lattice constant of 3.28 Å in our calculations. The GW[29] and GW + BSE[30] calculations were carried out using the BerkeleyGW package[28]. In the calculation of the electron self-energy, the dielectric matrix was constructed with a cutoff energy of 35 Ry. The dielectric matrix and the self-energy were calculated on an $18 \times 18 \times 1$ k-grid. The quasiparticle bandgap was converged to within 0.05 eV. In the calculation of the excitonic states, the quasiparticle band structure was interpolated onto a $180 \times 180 \times 1$ k-grid. The e–h interaction kernel was also calculated on the same grid. The 1*s* exciton binding energy was converged to within 0.1 eV. The spin–orbit coupling was included perturbatively within the LDA formalism.

Data availability. All data generated or analysed during this current study are available from the corresponding author on reasonable request.